arXiv:1601.05787v1 [physics.plasm-ph] 21 Jan 2016

First-Principles Equation of State Calculations of Warm Dense Nitrogen

K. P. Driver[1] and B. Militzer[1,2]

[1]*Department of Earth and Planetary Science, University of California, Berkeley, California 94720, USA**
[2]*Department of Astronomy, University of California, Berkeley, California 94720, USA*

(Dated: January 23, 2016)

Using path integral Monte Carlo (PIMC) and density functional molecular dynamics (DFT-MD) simulation methods, we compute a coherent equation of state (EOS) of nitrogen that spans the liquid, warm dense matter (WDM), and plasma regimes. Simulations cover a wide range of density-temperature space, $1.5 - 13.9$ g cm^{-3} and $10^3 - 10^9$ K. In the molecular dissociation regime, we extend the pressure-temperature phase diagram beyond previous studies, providing dissociation and Hugoniot curves in good agreement with experiments and previous DFT-MD work. Analysis of pair-correlation functions and the electronic density of states in the WDM regime reveals an evolving plasma structure and ionization process that is driven by temperature and pressure. Our Hugoniot curves display a sharp change in slope in the dissociation regime and feature two compression maxima as the K and L shells are ionized in the WDM regime, which have some significant differences from the predictions of plasma models.

PACS numbers:

I. INTRODUCTION

Nitrogen is a prototypical molecular system known for its large cosmological abundance, ability to form numerous chemical compounds, and its interesting solid, liquid, and electronic phase transitions at high pressures and temperatures[1,2]. Nitrogen can be found over a wide range of physical and chemical conditions throughout the universe, ranging from low densities in interstellar space[3] to extreme densities in stellar cores[4], and it plays important roles in planetary atmospheres[5] and interiors of ice giant planets[6]. In the condensed matter regime, nitrogen is capable of forming a wide variety of triple-, double-, and single-bonded compounds, which makes it of interest to geological and energy sciences. At higher densities and temperatures, nitrogen exists as a molecular fluid that undergoes a pressure-induced dissociation transition to polymeric and atomic fluids of interest in planetary science[7–9]. In the warm dense matter (WDM) regime, nitrogen exists in partially ionized plasma states, which are of fundamental interest to shock physics and astrophysics communities. An accurate understanding of the equation of state (EOS) in these regimes is important for determining the thermodynamic properties of the various nitrogen phases and their implications for science and technology.

At ambient conditions, nitrogen exists as a diatomic gas comprised of strong, triply-bonded dimers. At low T, nitrogen forms a molecular solid that undergoes a series of solid phase transitions with increasing pressure (see Fig. 1), which have been identified by a number of static compression experiments[10–15]. Around 50-70 GPa, density functional molecular dynamics (DFT-MD) simulations first predicted[16–21] the triple bond would destabilize to form various lower-energy, nonmolecular (possibly amorphous), polymeric phases composed of double- or single-bonded atoms, such as cubic gauche[18]. Later, static compression experiments confirmed the transition to nonmolecular phases[14,15,22–30]. The most extreme static compression experiments thus far have measured the equation of state up to a pressure of 270 GPa[24] and temperatures ranging up to 2,000 K[15]. First-principles simulations[18,20,21,31–39] have predicted solid molecular and nonmolecular phases up to pressures as high as 400 GPa[20]. However, first-principles predictions do not agree with experiments on what high pressure phases are stable at $T = 0$ K (Fig. 1), which continues to make solid nitrogen an interesting test case for improved experimental and theoretical methods.

While the solid phases have been intensely studied, the liquid, and, particularly the WDM and plasma states, have been investigated to a lesser extent. In this work, we focus on extending the studies of the EOS of liquid, WDM, and plasma states of nitrogen (Fig. 2). Several experimental measurements of dense, liquid nitrogen states have been performed using dynamic shock compression experiments[7,40–47], with the most extreme ones reaching up to a pressure of 180 GPa[47] and a temperature of 14,000 K[7]. The main focus of these experiments was to understand the shock-induced dissociation of molecular nitrogen at 30-80 GPa on the Hugoniot curve, as reviewed by Ross[1] and Nellis[2]. Nitrogen is also particularly interesting among the diatomic molecules because it exhibits unexpected phenomena, such as reflected-shock-induced cooling, where the dissociation to a polymeric fluid gives rise to a region of the phase diagram with $(\partial P/\partial T)_V < 0$ (Fig. 1). In this work, we revisit the dissociation curve and connect the liquid EOS to the WDM and plasma regimes.

Theoretical studies of shock-induced dissociation of dense, fluid nitrogen have been performed with a variety of approaches. A number of semi-empirical techniques have been employed, such as fluid variational theory[8,44,48–51], molecular dynamics[52], chemical equilibrium models[53–55], Monte Carlo[56], and integral equation theory[57]. First-principles DFT-MD has also been used to

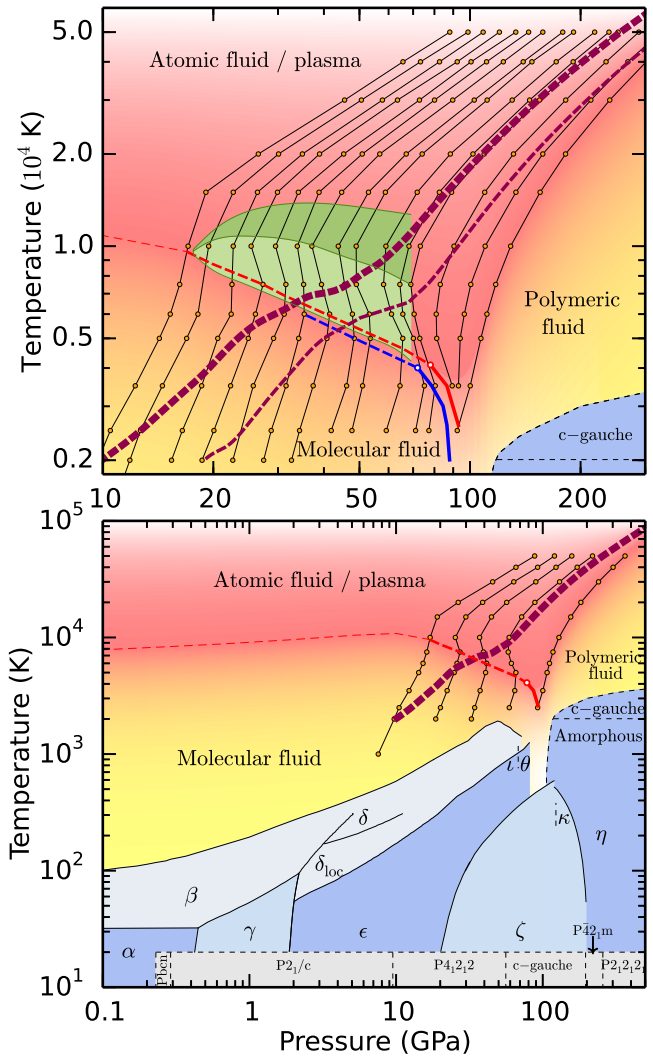

FIG. 1: Pressure-temperature phase diagram of nitrogen. The lower panel displays solid phases; molecular, polymeric, and atomic fluid phases; and the plasma regime. Phases well characterized by experiments are outlined with solid black lines, while others are outlined with a dashed line. Circles represent a subset of our DFT-MD isochore data used to compute the Hugoniot (thick, short-dashed curve) and dissociation curves. The latter changes from a dashed to solid curve to indicate the change to a first order liquid-liquid transition region. The upper panel is a magnified view of the molecular dissociation region, showing a larger subset of our DFT-MD calculations. The thick and thin dashed curves are our predicted Hugoniot curves for two different initial densities of 0.808 and 1.035 g cm^{-3}, respectively. Here, we also compare our dissociation curve with previous DFT-MD simulations by Boates *et al.*[9] (blue line). The green shaded area marks the region from the onset of dissociation, where the isochores begin to show that $(\partial P/\partial T)_V < 0$, to the point at which pressure returns to its value before the onset of dissociation.

study shocked, fluid states[58–60]. The semi-empirical and DFT-MD studies have been successful in predicting the principal Hugoniot curve and doubly shocked cooling within the dense, fluid dissociation regime (up to 110 GPa and 20,600 K)[58], in good agreement with the experimental measurements. In addition, Ross and Rogers[8] have used the activity expansion method (ACTEX)[61] to compute the Hugoniot curve in the plasma regime. ACTEX is a semi-analytic plasma model parameterized by spectroscopic data and is based on the grand partition function for a Coulomb gas of ions and electrons. It has been successful at predicting plasma properties in the weak-to-moderate coupling regime[62]. The ACTEX model identifies a Hugoniot curve compression maximum associated with K shell (1s) ionization, which will be discussed in more detail in Section VI.

DFT-MD has provided the most accurate description of liquid and warm dense states of nitrogen up to moderate temperatures ($\sim 10^5$ K). However, for higher temperature applications, such as astrophysical modelling and exploring pathways to fusion, a first-principles method that extends the EOS across the entire high energy density physics regime, bridging the liquid, WDM, and plasma regimes, is still needed. PIMC is one of the most promising first-principle methods to extend our study beyond the scope of DFT-MD because it is based on a quantum statistical many-body framework that naturally incorporates temperature effects and, in addition, becomes more efficient at higher temperatures. Building on earlier simulations of hydrogen[63–68] and helium[69–71], we have been extending the PIMC methodology for WDM composed of increasingly heavy elements[70,72–76]. Here, we apply our PIMC and DFT-MD simulations to liquid and WDM states of nitrogen over much wider density-temperature range (1.5–13.9 g cm^{-3} and 10^3–10^9 K, see Figs. 1 and 2) than has been previously explored with DFT-MD alone.

The paper is organized as follows: In Section II, we describe PIMC and DFT-MD simulation methods for liquid and WDM regimes. In Section III, we first discuss the DFT-MD calculations of the liquid EOS, its dissociation transition, and present an updated phase diagram. We then extend the liquid EOS into the WDM and plasma regimes and show that DFT-MD and PIMC produce consistent results for intermediate temperatures. In section IV, we characterize the structure of the plasma and ionization processes by examining changes in different pair-correlation functions as a function of temperature and density. In section V, we discuss the electronic density of states to provide further insight into the ionization process. In section VI, we discuss shock Hugoniot curves. Finally, in section VII, we summarize our findings.

II. SIMULATION METHODS

PIMC[77–79] is a state-of-the-art first-principles method for computing the properties of interacting quantum systems at finite temperature. Since PIMC is based on the

thermal density matrix formalism, it naturally incorporates temperature into the framework. The density matrix is expressed in terms of Feynman's imaginary time path integrals, which are evaluated by efficient Monte Carlo techniques, treating electrons and nuclei equally as quantum paths that evolve in imaginary time without invoking the Born-Oppenheimer approximation. Therefore, PIMC is able to explicitly treat all the effects of bonding, ionization, exchange-correlation, and quantum degeneracy in a many-body framework that simultaneously occur in the WDM regime[80]. The Coulomb interaction is incorporated via pair density matrices derived from the eigenstates of the two-body Coulomb problem[81,82]. The efficiency of PIMC increases with temperature as particles behave more classically at higher temperatures and fewer time slices are needed to describe quantum mechanical many-body correlations.

PIMC requires a minimal number of controlled approximations, which are minimized by converging the time step and system size. We determined the necessary time step by converging total energy until it changed by less than 1.0%. We use a time step of 1/256 Ha^{-1} for temperatures below 4×10^6 K. For higher temperatures, we decreased the time step as 1/T. In order to study finite size errors, we perform simulations with 8 and 24 atoms in cubic simulations cells and found that the total energy differed by 0.4% or less[75]. All results for the internal energy and pressure that we report have statistical errors of 0.3% or less.

The only uncontrolled approximation in PIMC is the fixed-node approximation that is introduced to avoid the fermion sign problem[83]. We employ a free-particle nodal structure, which we have shown to work reliably for partially ionized hydrogen[67], helium[70], carbon[72], water[72], oxygen[74], and neon[75]. Free-particle nodes work well as long as only a small number of bound electronic states are occupied. For plasmas of first-row elements, we have found that free particle nodes yield good results for conditions where the 1s states are fully occupied and the 2s states are partially occupied[72]. Lower temperature conditions can be studied efficiently with DFT-MD.

DFT-MD[85] is an efficient, state-of-the-art, first-principles method for zero and low temperatures ($T < 1\times10^6$ K). DFT formalism provides a mapping of the many-body problem onto a single-particle problem with an approximate exchange-correlation potential to describe many-body effects. In the WDM regime, where temperatures are at or above the Fermi temperature, the exchange-correlation functional is not explicitly designed to accurately describe the electronic excitations[86]. However, in our previous PIMC and DFT-MD work[72], we found existing DFT functionals to be sufficiently accurate even at high temperatures.

DFT incorporates effects of finite electronic temperature by using a Fermi-Dirac function to smear out the thermal occupation of single-particle electronic states[87]. As temperature grows large, an increasing number of bands are required to account for the occupation of excited states in the continuum, which typically causes the efficiency of the algorithm to become intractable at temperatures beyond 1×10^6 K. In addition, pseudopotentials replace the core electrons in each atom to improve efficiency. Here, we are careful to avoid using DFT-MD at temperatures where the K shell electrons undergo excitations and study those conditions with PIMC instead.

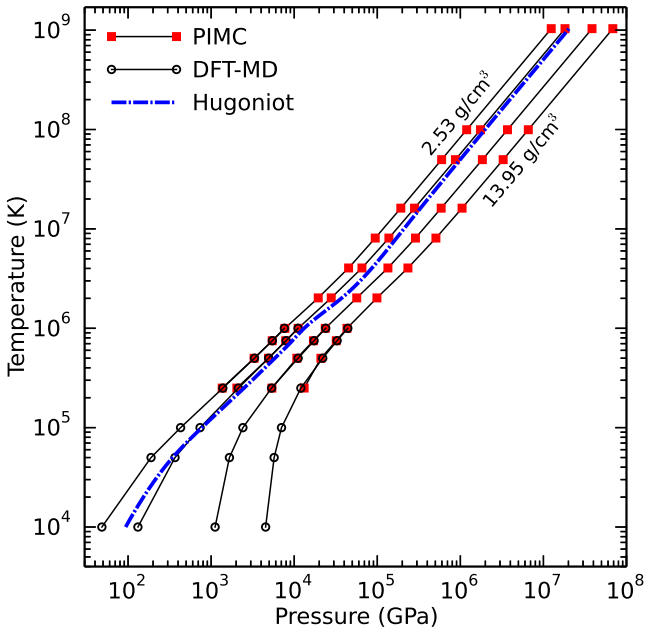

FIG. 2: Temperature-pressure isochores computed with DFT-MD (circles) and PIMC (squares) at densities of 2.5, 3.7, 7.8, and 13.9 g cm^{-3}. The blue dash-dotted line shows the Hugoniot curve for an initial density of $\rho_0 = 1.035$ g cm^{-3}

Progress has been made in orbital-free (OF) DFT and average-atom DFT methods, which introduce additional approximations beyond standard Kohn-Sham DFT-MD in order to improve the efficiency of the scaling with temperature. OF-DFT approximates the free energy of the homogeneous electron gas by a functional that is independent of the single-particle orbitals[88,89]. The speed-up gained has resulted in an significant trade-off in accuracy, but recent OF-DFT developments have shown the method is potentially capable of being competitive with KS-DFT[90,91]. In an effort to make even greater gains in efficiency, DFT-based average-atom models make further approximations based on solving for the electronic properties of a single atom within the plasma[92]. Such models have been shown to predict the electronic structure of the isolated atoms well, and recent developments have begun a more consistent treatment of many-body systems[93]. OF-DFT and average-atom models are capable of simulating systems sizes up to a few hundred particles, but ultimately, along with DFT-MD, they are based on a ground-state framework, and it is important to develop more accurate, finite-temperature methods with fewer approximations, such as PIMC, to benchmark such cal-

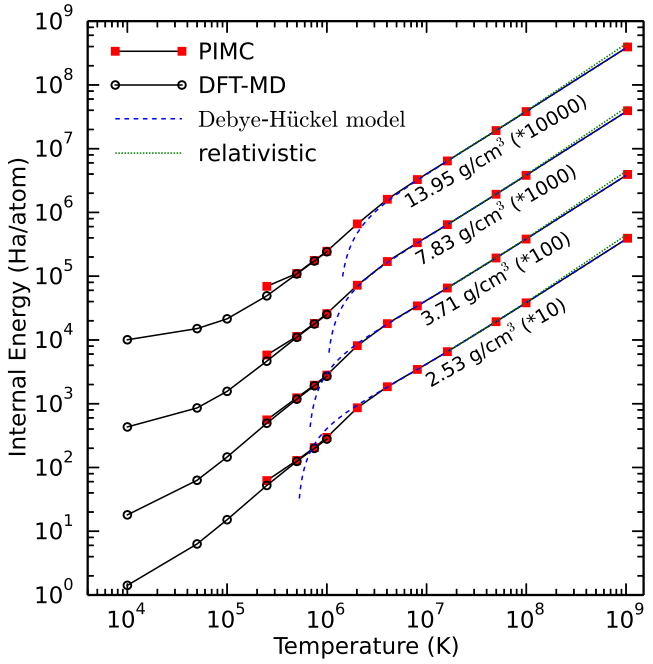

FIG. 3: Isochores computed with PIMC (squares), DFT-MD (circles), and the Debye-Hückel model (dashes) at four densities. The high-temperature relativistic correction is shown as a dotted line. To improve visibility on a log scale, the energies of the four isochores have been shifted by the N_2 molecule energy, −54.614969 Ha/atom, and multiplied by factors of 10, 100, 1,000, and 10,000 as indicated in the labels. The original energies are given in the Supplementary Material[84].

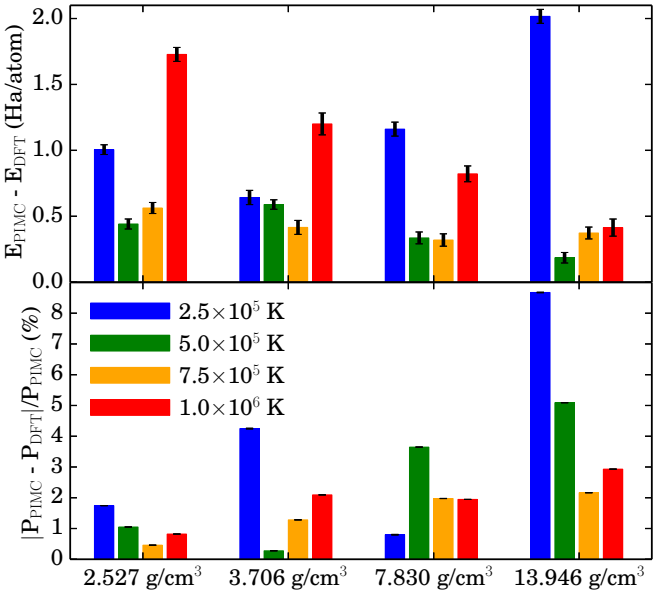

FIG. 4: Differences in PIMC and DFT-MD energies and pressures. The top panel shows energy differences, while the bottom panel shows the absolute relative error of pressure in per cent. One-σ errors in the differences are shown in black.

culations.

We employ standard Kohn-Sham DFT-MD simulation techniques for our calculations of liquid and WDM matter states. Simulations are performed with the Vienna *Ab initio* Simulation Package (VASP)[94] using the projector augmented-wave (PAW) method[95], and a NVT ensemble, regulated with a Nosé-Hoover thermostat. Exchange-correlation effects are described using the Perdew-Burke-Ernzerhof[96] generalized gradient approximation. Electronic wave functions are expanded in a plane-wave basis with a energy cut-off as high as 2000 eV in order to converge total energy. For liquid simulations, we used 64-atom supercells with a time-step of 1.5 fs. For WDM calculations, size convergence tests up to a 24-atom simulation cell at temperatures of 10,000 K and above indicate that total energies are converged to better than 0.1% in a 24-atom simple cubic cell. We find, at temperatures above 250,000 K, 8-atom supercell results are sufficient since the kinetic energy far outweighs the interaction energy at such high temperatures[75]. The number of bands in each calculation is selected such that thermal occupation is converged to better than 10^{-4}, which requires up to 8,000 bands in a 24-atom cell at 1×10^6 K. All simulations are performed at the Γ-point of the Brillouin zone, which is sufficient for high temperature fluids, converging total energy to better than 0.01% relative to a comparison with a converged grid of k-points.

III. EOS OF LIQUID, WDM, AND PLASMA PHASES

In this section, we report our DFT-MD and PIMC EOS results for the liquid, WDM, and plasma regimes. The Supplementary Material[84] provides all of our computed pressure and energy data. The VASP DFT-MD energies have been shifted by −54.3064682071 Ha/atom in order to bring the PAW-PBE pseudopotential energy in alignment with all-electron DFT calculations. The shift was calculated by performing an all-electron atomic calculation with the OPIUM code[97] and a corresponding isolated-atom calculation in VASP.

In the liquid regime, we computed isochores with DFT-MD on a dense grid of 15 densities spanning conditions from 1.5–3.7 g cm^{-3} and 10^3–5×10^4 K, in order to accurately map out the molecular dissociation transition. We extend the work of Boates *et al.*[9] to higher temperatures and lower pressures. Our pair-correlation curves agree with the experimental molecular bond length of 1.1 Å at low temperature and are generally consistent with the work of Boates *et al.* Our dissociation curve was constructed by determining the temperature at which the molecular lifetime reached 0.2 ps, which is the same cut-off for molecular stability used by Boates and limits it to 15 vibrations. Consistent with previous work[7,9,43,45,59],

we find $(\partial P/\partial T)_V < 0$ in the dissociation region with a first order dissociation transition at pressures near 78-90 GPa. Below 18 GPa, we find no $(\partial P/\partial T)_V < 0$ region exists.

Fig. 1 shows the pressure-temperature phase diagram with our dense grid of DFT-MD isochores in the liquid region, as well as the dissociation and Hugoniot curves. The lower panel of Fig. 1, which includes a subset of our DFT-MD isochores, shows the phase diagram ranging from solid to low-temperature plasma phases. The solid phase boundaries, outlined with solid lines, are reproduced from a variety of experiments[11–15,98–100]. The melting curve is also reproduced from experiments[98–100], which agrees with DFT-MD calculations[101], and displays a negative slope with a triple point near 90 GPa and 1000 K. We include phases that have been predicted to be stable by a DFT random structure searching algorithm at T=0 K[20], which have not been seen by experiment.

The upper panel Fig. 1 is a magnified view of the dissociation region, displaying a larger subset of the DFT-MD isochores performed in our study. The molecules may dissociate into polymeric or atomic fluid through a first order phase transition, marked by the solid portion of dissociation line in the figure. As pressure decreases, the dissociation curve reaches a critical point near 78 GPa and 4100 K, marked by a white dot and a change to a dashed line to indicate the transition is no longer first order. Starting at 18 GPa, where our DFT-MD data ends, we constructed a free energy model[102] with noninteracting atoms and molecules that extends the dissociation curve to low pressures, marked by a thin, dashed line. We postpone the discussion of the liquid Hugoniot until Section VI.

In order to extend our nitrogen EOS into the WDM and plasma regimes, we compute additional isochore data with DFT-MD and PIMC for temperatures ranging up to 10^9 K for four of the densities (2.5, 3.7, 7.8, and 13.9 g cm^{-3}). Fig. 2 shows the data computed for the four isochores and compares pressures obtained for nitrogen from PIMC and DFT-MD. Likewise, Fig. 3 compares internal energies and also compares with results from the Debye-Hückel model[103], constructed for the fully ionized plasma. Using a relativistic, fully-ionized model[104], we also show the magnitude of the relativistic correction to the internal energy, which results in a 14% change at the high-temperature limit. There is not a significant relativistic correction to the pressure. In both pressure and energy, we find good agreement between PIMC and DFT-MD results in the temperature range of $5.0\times10^5-1\times10^6$ K. At a temperature of 2.5×10^5 K, the PIMC free-particle nodes start to become insufficient for describing bound electronic states, and the results begin to deviate significantly from that of DFT-MD. At high temperature, the PIMC pressures and energies converge to the weakly interacting plasma limit, in agreement with the classical Debye-Hückel model.

Fig. 4 shows the differences between the PIMC and DFT-MD pressures and energies as a function of temperature in the overlap regime where both methods operate efficiently. DFT-MD and PIMC internal energies differ by at most 2 Ha/atom and pressures differ by less than 8% in the temperature range of $2.5\times10^5-1\times10^6$ K. The size of the discrepancy between our PIMC and DFT-MD results also places an approximate limit on the magnitude of the correction that a new free-energy functional, such as those used in OF-DFT, can change existing KS-DFT results. Typically, the error is largest at the lowest and highest temperatures. This is possibly because, at low temperature, the PIMC free-particle nodes are expected to breakdown, while, at high temperature, the DFT exchange-correlation functional and pseudopotential may breakdown. The pseudopotential, with a frozen 1s core, may also begin to leave out excitation effects at temperatures close to 10^6 K. In our previous studies, we found it is not uncommon for one third of the energy discrepancy at 10^6 K to be attributed to pseudopotential error[72,74,75].

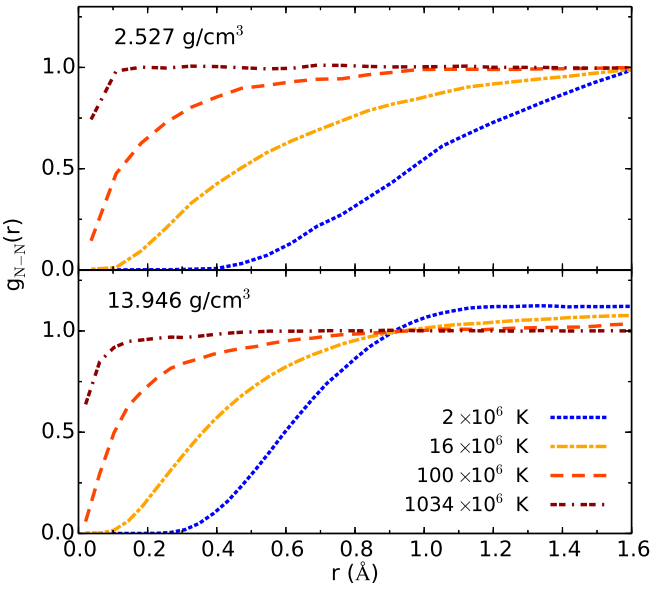

FIG. 5: Nuclear pair-correlation functions for nitrogen from PIMC over a wide range of temperatures and densities.

Together, Figs. 2 and 3 show that the DFT-MD and PIMC methods form a coherent EOS over all temperatures ranging from condensed matter to the WDM and plasma regimes. The good agreement between PIMC and DFT-MD indicates that DFT exchange-correlation potential remains valid even at high temperatures and that the PIMC free-particle nodal approximation is valid as long as the 2s state is sufficiently ionized. The analytic Debye-Hückel models agree well with PIMC at high temperatures, but the Debye-Hückel model does not include bound states and, therefore, cannot describe low temperatures.

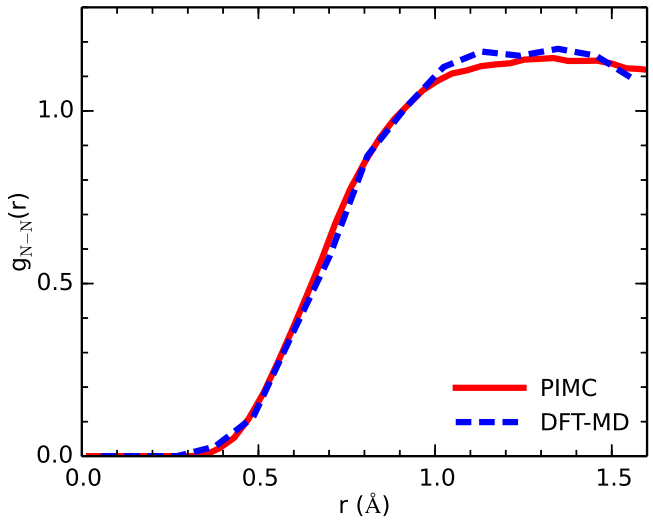

FIG. 6: Comparison of PIMC and DFT nuclear pair-correlation functions for nitrogen at a temperature of 1×10^6 K and a density of 13.946 g cm^{-3}.

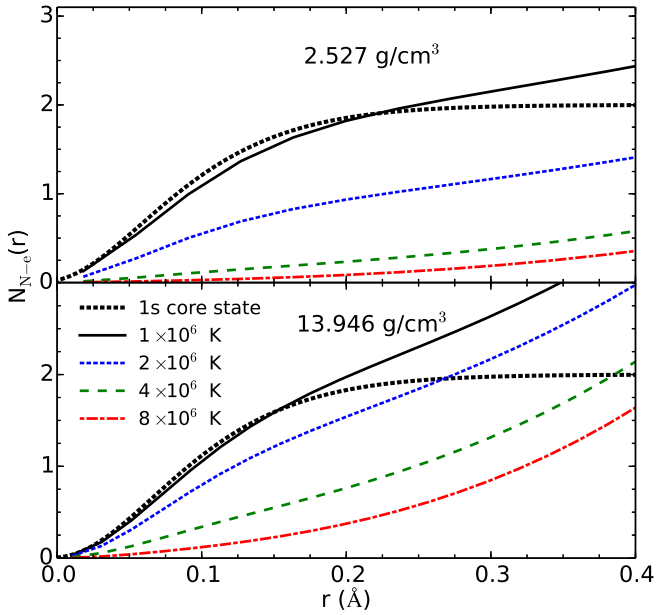

FIG. 7: N(r) function representing the number of electrons contained in a sphere of radius, r, around an nitrogen nucleus. PIMC data at four temperatures is compared with the analytic 1s core state.

IV. PAIR-CORRELATION FUNCTIONS

In this section, we study pair-correlation functions[105] in order to understand the evolution of the fluid structure and ionization in nitrogen plasmas as a function of temperature and density.

Fig. 5 shows the nuclear pair-correlation functions, $g(r)$, computed with PIMC over a temperature range of $2\times10^6 - 1.034\times10^9$ K and for densities of 2.527 and 13.946 g cm^{-3}. Atoms are kept farthest apart at low temperatures due to a combination of Pauli exclusion among bound electrons and Coulomb repulsion. As temperature increases, kinetic energy of the nuclei increases, making it more likely to find atoms at close range. In addition, the atoms become increasingly ionized, which gradually reduces the Pauli repulsion, but increases the ionic Coulomb repulsion. As density increases, the likelihood of finding two nuclei at close range slightly rises. At high temperatures, the system approaches the Debye-Hückel limit, behaving like a weakly correlated system of screened Coulomb charges.

Fig. 6 compares the nuclear pair-correlation functions of PIMC and DFT-MD at a temperature of 1×10^6 K in an 8-atom cell at a density of 13.946 g cm^{-3}. The overlapping $g(r)$ curves verify that PIMC and DFT predict consistent structural properties.

Fig. 7 shows the integral of the nucleus-electron pair correlation function, $N_{N-e}(r)$, which represents the average number of electrons within a sphere of radius r around a given nucleus. At the lowest temperature, 1×10^6 K, we find that the 1s core state is always fully occupied, as it agrees closely with the result of an isolated 1s state. As temperature increases, the atoms are gradually ionized and electrons become unbound, causing $N_{N-e}(r)$ to decrease. At higher density, an even higher temperature is required to fully ionize the atoms, indicating that the 1s ionization fraction decreases with density.

There are two important physical points to note about this result. First, it is clear that 1s ionization fraction is not affected by pressure ionization in the considered density range, which is supported by the fact that the nuclei are not yet close enough for Pauli exclusion to trigger the ionization of the 1s state. Pauli exclusion effects decay on the scale of ~ 0.04 Å (size of 1s orbital), while Fig. 6 shows that the nuclei remain at least 0.3 Å apart at our highest density. Secondly, we note that in our work on dense oxygen[74] we performed all-electron DFT-MD calculations and found that the 1s ionization fraction for a fixed temperature decreases because the Fermi energy shifts to higher energies more rapidly than the 1s state shifts towards the continuum when density increases. Thus, the decrease in the 1s ionization fraction in Fig. 7 at a fixed temperature with increasing density is due to a rapid shift of the Fermi energy. Eventually, the 1s ionization fraction will increase when density is high enough to push the 1s states into the continuum, but we have not studied such densities here.

Fig. 8 shows electron-electron pair correlations for electrons having opposite spins. The function is multiplied by the density ρ, so that the integral under the curves is proportional to the number of electrons. The electrons are most highly correlated for low temperatures, which reflects that multiple electrons occupy bound states around a given nucleus. As temperature increases, electrons are thermally excited, decreasing the

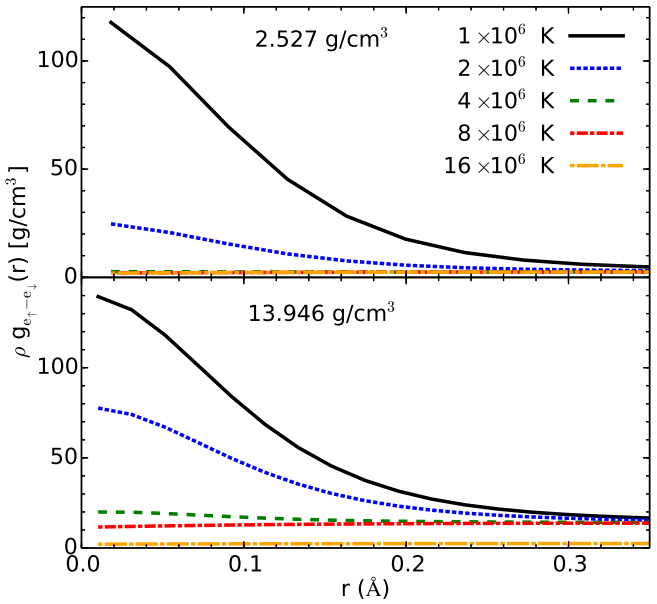

FIG. 8: The electron-electron pair-correlation functions for electrons with opposite spins computed with PIMC.

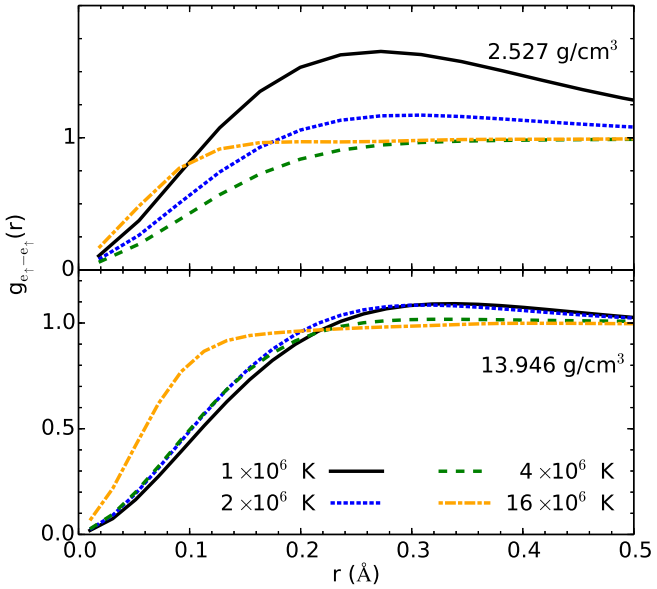

FIG. 9: The electron-electron pair-correlation functions for electrons with parallel spins computed with PIMC.

correlation among each other. The positive correlation at short distances increases with density, consistent with a lower ionization fraction.

Fig. 9 shows electron-electron pair correlations for electrons with parallel spins. The positive correlation at intermediate distances reflects that different electrons with parallel spins are bound to a given nucleus. For short separations, electrons strongly repel due to Pauli exclusion and the functions decay to zero. As density increases, the peak at intermediate distances decreases, which clearly shows the effect of pressure ionization on the L shell. These orbitals are much larger than the 1s state and are therefore subject to Pauli exchange with nearby nuclei. As temperature increases, electrons become less bound, which also causes the correlation to become more like an ideal fluid.

V. ELECTRONIC DENSITY OF STATES

In this section, we report DFT-MD results for the electronic density of states (DOS) as a function of temperature and density in order to gain further insight into temperature and pressure ionization effects.

Fig. 10 shows the total and occupied DOS at two temperatures and two densities. Results were obtained by averaging over ten uncorrelated snapshots chosen from a DFT-MD trajectory. Smooth curves were obtained by using a 4×4×4 k-point grid and applying a Gaussian smearing of 2 eV. The eigenvalues of each snapshot were shifted so that the Fermi energies align at zero. The integral of the DOS is normalized to 1.

At low temperature and density, the general structure is composed of two peaks below the Fermi energy, representing the atomic 2s and 2p states. The peaks broaden and merge at higher temperatures and densities as they become ionized. For higher density, the total DOS resembles that of an ideal plasma. For lower densities, a dip in the DOS indicates beginning of the continuous spectrum of conducting states. At the lowest temperature ($\sim 10^4$ K) shown for each density, the majority of occupied states lie below the Fermi energy. At the higher temperature ($\sim 10^5$ K), a significant fraction of the occupied states now lie above the Fermi energy as the second shell becomes ionized. Finally, we note that the Fermi energy plays the role of the chemical potential in the Fermi-Dirac distribution, which shifts towards more negative values as the temperature is increased. Because we subtract the Fermi energy from the eigenvalues, the peak shifts to higher energies with increasing temperature. The fact that the peaks are embedded into a dense, continuous spectrum of eigenvalues indicates that they are conducting states.

VI. SHOCK COMPRESSION

Dynamic shock compression experiments allow one to measure the EOS and other physical properties of hot, dense fluids. Such experiments are often used to determine the principal Hugoniot curve, which is the locus of final states that can be obtained from different shock velocities. A number of Hugoniot measurements have been made for nitrogen[7,41–43,45–47]. Density functional theory has been validated by experiments as an accurate tool for predicting the shock compression of a variety of different materials[106,107], including nitrogen[58,59].

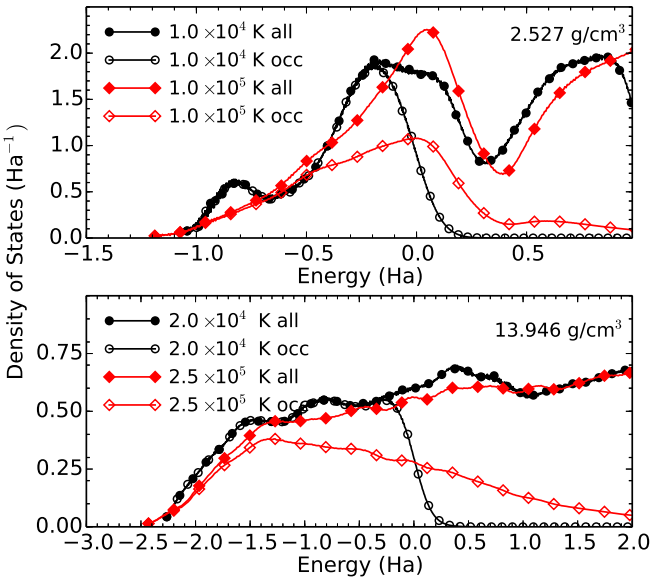

FIG. 10: Temperature dependence of the total (all) and occupied (occ) electronic DOS of dense, fluid nitrogen at densities of 2.53 and 13.95 g cm^{-3}. Each DOS curve has had the relevant Fermi energy for each temperature subtracted from it.

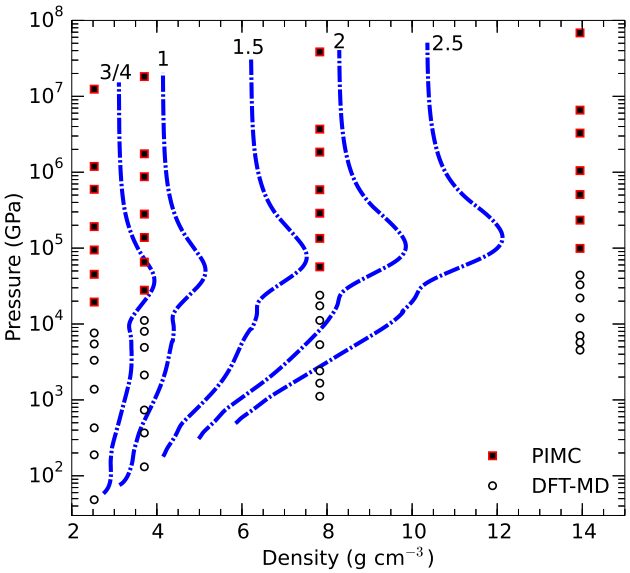

FIG. 11: Shock Hugoniot curves for different initial densities ranging from 0.75- to 2.5-fold the density of solid N_2, 1.035 g cm^{-3}, at ambient pressure.

In the course of a shock wave experiment, a material whose initial state is characterized by an internal energy, pressure, and volume (E_0, P_0, V_0) will change to a final state denoted by (E, P, V) while conserving mass, momentum, and energy. This leads to the Rankine-

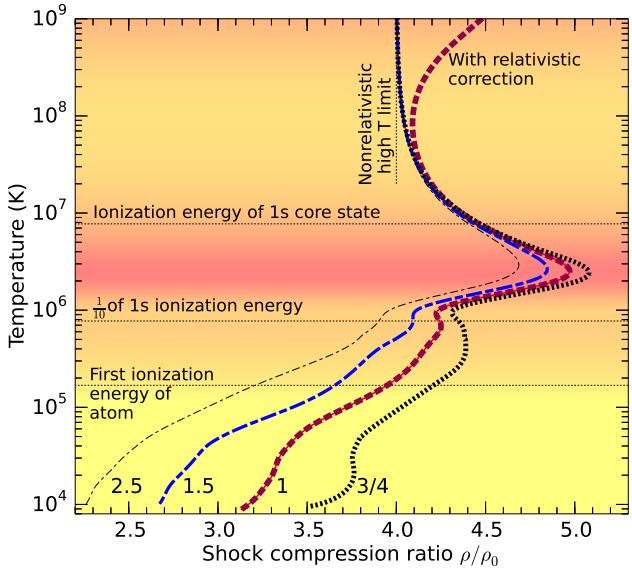

FIG. 12: Hugoniot curves as a function of the shock compression ratio for different initial densities as plotted in Fig. 11. The 1-fold curve is shown with (dashed line) and without (solid line) the relativistic correction. The dark shaded marks the temperature range of highest compression.

Hugoniot relation[108],

$$(E - E_0) + \frac{1}{2}(P + P_0)(V - V_0) = 0. \qquad (1)$$

Here, we compute the Hugoniots from the first-principles EOS data reported in the Supplementary material[84]. The pressure and internal energy data points were interpolated with bi-cubic spline functions in $\rho - T$ space. For the initial state, we used the energy of an isolated ($P_0 = 0$) nitrogen molecule, $E_0 = -109.2299$ Ha/N_2. V_0 was determined by the density, $\rho_0 = 1.035$ g cm^{-3}, of solid nitrogen in the $Pa\bar{3}$ phase[109]. The resulting Hugoniot curve has been plotted in T-P and P-ρ spaces in Figs. 2 and 11, respectively.

Samples in shock wave experiments may be precompressed inside of a diamond anvil cell in order to reach much higher final densities than are possible with a sample at ambient conditions. This technique allows shock wave experiments to probe density-temperature consistent with planetary and stellar interiors[110]. Therefore, we repeated our Hugoniot calculation starting with initial densities ranging from a 0.75 to a 2.5-fold of the density typically used in shock-compression experiments (0.808 g cm^{-3}). Fig. 11 shows the resulting family of Hugoniot curves. While starting from an initial density of 0.808 g cm^{-3} leads to a maximum shock density of 5.15 g cm^{-3} (4.97-fold compression), a 2.5-fold precompression yields a much higher maximum shock density of 12.13 g cm^{-3} (4.69-fold compression). Alternatively, such extreme densities can be reached with double and triple shock experiments.

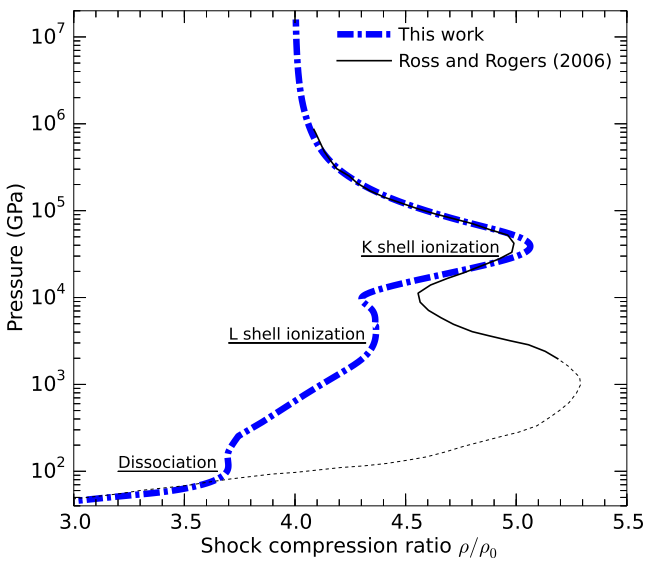

FIG. 13: Comparison of our combined PIMC and DFT-MD Hugoniot curve with predictions of ACTEX plasma model calculations by Ross and Rogers[8]. The dashed line portion of the plasma model curve indicates where the ACTEX results were interpolated to match experimental data below 100 GPa. The initial density was $\rho_0 = 0.8076$ g cm^{-3} (V_0= 28.80 Å^3/atom).

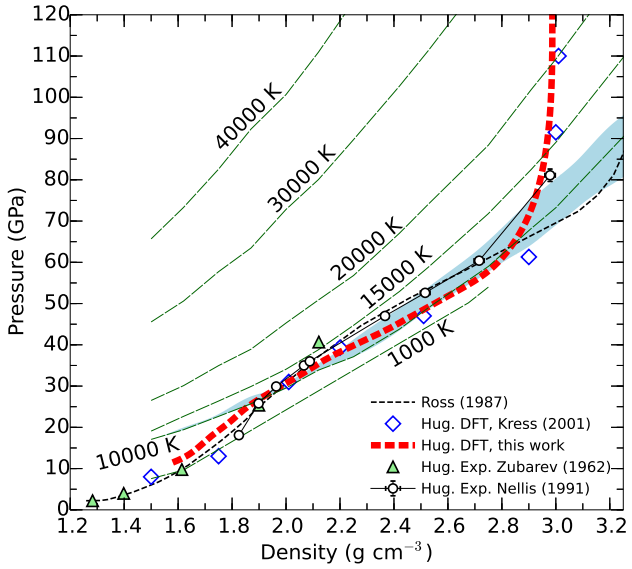

FIG. 14: Comparison of the liquid DFT-MD Hugoniot with the experiments of Nellis *et al.*[7] and Zubarev *et al.*[40] and the theory of Ross *et al.*[49] (variational fluid theory) and Kress *et al.*[58] (DFT-MD). The blue shaded region indicates the region of dissociation with $(\partial P/\partial T)_v < 0$ in the phase diagram of Fig. 1. Our Hugoniot passes through this region, but there is no evidence of cooling along the principal Hugoniot curve. The green dashed lines show isotherms from our DFT-MD simulations.

Fig. 12 shows the temperature dependence of the shock-compression ratio for the four representative Hugoniot curves from Fig. 11. In the high-temperature limit, all curves converge to a compression ratio of 4, which is the value of a nonrelativistic, ideal gas. We also show the magnitude of the relativistic correction to the Hugoniot in the high-temperature limit. The shock compression and structure along the Hugoniot is determined by the excitation of internal degrees of freedom, such as dissociation and ionization processes, which increases the compression, and, in addition, the interaction effects, which decrease the compression[69]. Consistent with our studies of other elements, we find that an increase in the initial density leads to a slight reduction in the shock compression ratio (Fig. 12) because particles interact more strongly at higher density.

For the lowest two initial densities, the shock compression ratio in Fig. 12 exhibits two maxima as a function of temperature, which can be attributed to the ionization of electrons in the K (1s) and L (2s+2p) shells. On the principal Hugoniot curve, the first maximum of ρ/ρ_0=4.26 occurs at temperature of 6.77×10^5 K (58.3 eV) , which is well above the first and second ionization energies of the nitrogen atom, 14.53 and 29.60 eV. A second compression maximum of ρ/ρ_0=4.97 is found for a temperature of 2.55×10^6 K (220 eV), which can be attributed to a substantial ionization of the 1s core states. For an isolated nitrogen atom, the 1s ionization energy is 667.05 eV. However, fractional ionization is expected to occur at much lower temperature already. This is consistent with

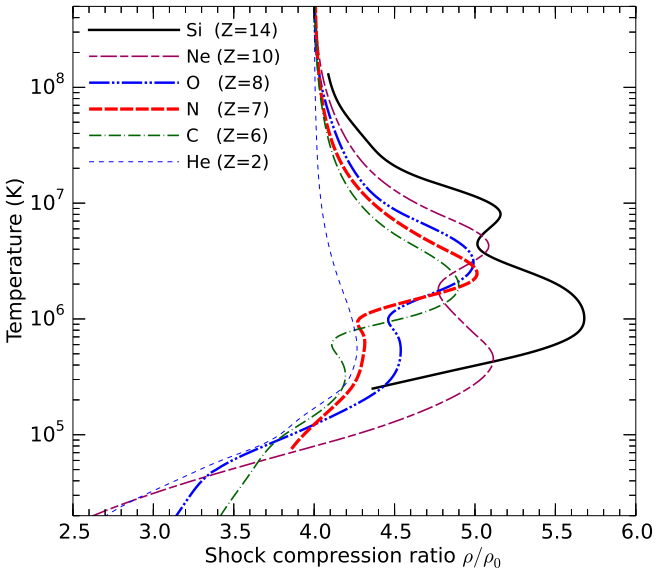

FIG. 15: Comparison of the shock Hugoniot curves for different materials. The initial volume V_0 has been chosen such that the density of the electrons is the same for all materials (V/N_e = 3.586 Å^3). The various maxima in compression corresponds to excitations of electrons in the first and second electron shells.

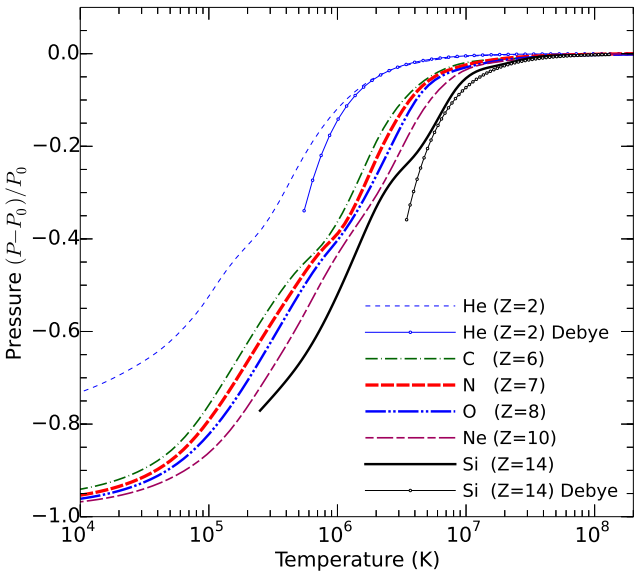

FIG. 16: Pressure vs. temperature is shown for isochores of different materials. The pressure of a fully-ionized, non-interacting plasma, P_0, has been removed in order to compare the excess pressure due to interactions. The densities have been chosen such that electronic density is the same for all materials ($V/N_e = 0.8966$ Å^3). This electronic density corresponds to the high-temperature limit of 4-fold compression of the shock Hugoniot curves in Fig. 15. The Debye model has been included for helium and silicon.

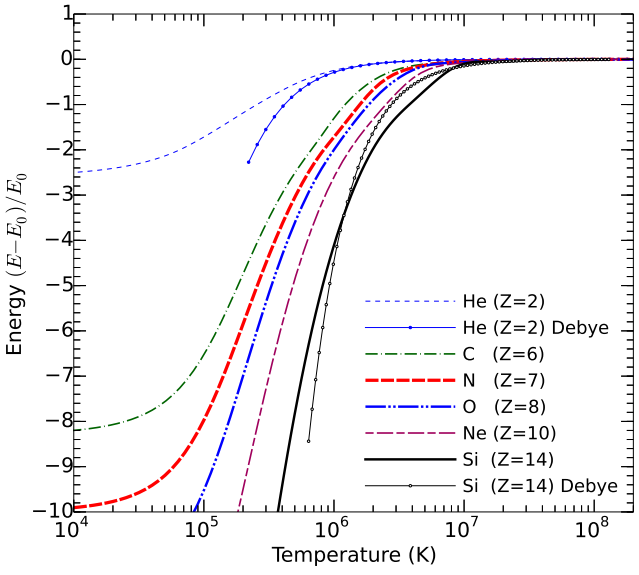

FIG. 17: Internal energy vs. temperature is shown for the isochores in Fig. 16. The energy contribution from a fully-ionized, non-interacting plasma, E_0, has been removed in order to compare only the interaction effects.

the ionization process we observe in Fig. 7, where the charge density around the nuclei is reduced over the range of $2 - 8 \times 10^6$ K. Since DFT-MD simulations, which use pseudopotentials to replace core electrons, cannot access the regime of core ionization, both PIMC and DFT-MD are needed to determine all features along the principal Hugoniot curve.

Fig. 13 compares our combined PIMC and DFT-MD Hugoniot curve with predictions from the ACTEX calculations by Ross and Rogers[8]. We find very good agreement for P $\geq$ 20,000 GPa, which includes a compression peak due to the ionization of K shell and confirms the strengths of the ACTEX method in highly ionized regimes with weak-to-moderate Coulomb coupling. While the K shell peak pressures agree almost perfectly in pressure, the ACTEX predicts a maximum compression ratio that is 0.07 lower than predicted by our PIMC simulations. In the pressure range from 2,000 to 20,000 GPa, where ionization of the L shell occurs, we find that the ACTEX model substantially overestimates the shock compression. In the range of 100 to 2000 GPa (dashed line in Fig. 13), Ross and Rogers interpolated their Hugoniot curve based on a collection of previous ACTEX calculations for other light elements[62] and available experimental data below 100 GPa[7]. Therefore, it is not too surprising that PIMC and the analytic model disagree by up to 20% in the pressure. The comparison shows the importance of using first-principles methods such as PIMC and DFT-MD to correctly predict the ionization compression peaks of the Hugoniot curve in more strongly coupled regimes. With DFT-MD, we are also able to capture the sharp change in slope in the Hugoniot curve, which is associated with dissociation as internal energy is absorbed to break the molecular bond.

Fig. 14 shows a magnified view of the low-pressure Hugoniot in the dissociation region. Our DFT-MD Hugoniot generally agrees well with the experimental data of Nellis *et al.*[7] and previous DFT-MD calculations[58]. DFT-MD accurately captures the sharp increase in compressibility in the dissociation transition region, while the Ross model underestimates the compressibility more or less depending on the parameterization[49]. Slight deviations with experiment tend to lie near the region of $(\partial P/\partial T)_V < 0$, marked by the blue shaded region. The discrepancy could either be due to impedance matching difficulties in experiment or shortcomings of DFT-MD approximations. A negative $(\partial P/\partial T)_V$ region and molecular dissociation can, in principle, trigger a shock wave to split into two separate waves[111]. This occurs when the shock speed is not monotonously increasing with particle speed. However, this is not predicted to occur based on our DFT-MD EOS, and we find it unlikely that this hypothesis can explain the discrepancy between the theoretical and experimental results in Fig. 14. We also note that including zero point motion has a negligible affect on the Hugoniot curve.

VII. EOS COMPARISON OF FIRST- AND SECOND-ROW PLASMAS

Using PIMC and DFT-MD, we have computed the first principles EOS and shock Hugoniot curves for several materials in the the WDM and dense, plasma regime. In this section, we compare our collective sets of data and discuss some of the trends we have observed.

Fig. 15 compares our computed shock Hugoniot curves from simulations of He[70], C[72], O[74], Ne[75], and Si[76] in the WDM and plasma regimes. The Hugoniot curve comparison shows distinct compression maxima for all materials, but the maxima and structure along the Hugoniot depend strongly on the atomic number, Z, which is directly connected to internal degrees of freedom and interaction effects[69]. We find the shock Hugoniot compression maxima, corresponding to K and L shell ionization, increase in both compression and temperature with the atomic number, Z. This is not unexpected because the binding energy scales as Z^2, which means a higher temperature is needed to reach the regime of ionization. When this happens, a larger energy difference, $E - E_0$, must be compensated by the $P(V - V_0)$ term in Eq. 1. Even though the pressure increases with ionization also, we still see a higher shock compression for higher Z materials in Fig. 15.

Figs. 16 and 17 compare the pressure and internal energies of the same set of materials in the Hugoniot curve comparison. The plots compare the excess pressure and energy, where the ideal Fermi gas contributions have been removed in order to compare only interaction effects, which become important for $T < 10^8$ K when electrons start to occupy the K shell. For higher Z, this occurs at higher temperature, which explains the trends seen in Figs. 15-17. The Debye model can capture only the high temperature limit of this trend since it cannot describe the occupation of the K shell. There is a visible softening of the slope in the pressure and internal energy curves for temperatures around 10^6 K, which corresponds to the intermediate regime between K and L shell ionization. As expected, the onset of the slope-softening occurs at higher temperatures for higher Z elements.

We note that, for each material, that we have computed consistent, overlapping results with both DFT-MD and PIMC at temperatures near 10^6 K. The agreement implies that our zero-temperature, DFT exchange-correlation potential (PBE) remains valid for a large set of materials at high temperatures and that the free-particle nodal approximation is accurate in PIMC when the K shell electrons are bound and L-shell is partially ionized.

VIII. CONCLUSIONS

In this work, we have used DFT-MD and PIMC to compute liquid and WDM states of nitrogen to provide an EOS witch bridges the condensed matter and warm dense matter regimes. In the liquid regime, we have extended the phase diagram beyond previous studies by computing the dissociation curve for a broader region of conditions and extending the Hugoniot to the WDM regime. In the WDM regime, we have combined PIMC with DFT-MD to construct a coherent EOS for nitrogen over a wide range of densities and temperatures. The two methods produce consistent pressures and energies in temperature range of 5.0×10^5–1×10^6 K. At high temperatures, our EOS converges to the analytic Debye-Hückel result for weakly interacting plasmas. Nuclear and electronic pair-correlations reveal a temperature- and pressure-driven ionization process, where temperature-ionization of the 1s state is suppressed, while other states are efficiently ionized as temperature and density increases. Temperature-density dependence of the electronic density of states confirms the temperature- and pressure-ionization behavior observed in the pair-correlation data. Lastly, we find the ionization imprints a signature on the shock Hugoniot curves and that PIMC simulations are necessary to determine the state of the highest shock compression. By combining our liquid DFT-MD data with our WDM data, we provide a first-principles Hugoniot that matches experiment at low pressures and extends to the classical plasma regime. Our Hugoniot and equation of state will help to build more accurate models for astrophysical applications and energy applications.

Acknowledgments

This research is supported by the U. S. Department of Energy, grant de-sc0010517. Computational support was provided by NERSC and the Janus supercomputer, which is supported by the National Science Foundation (Grant No. CNS-0821794), the University of Colorado, and the National Center for Atmospheric Research.

* Electronic address: kdriver@berkeley.edu; URL: `http://militzer.berkeley.edu/~driver/`

[1] M. Ross, High Press. Res. **16**, 371 (2000).
[2] W. J. Nellis, J. Phys. Condens. Matter **14**, 11045 (2002).
[3] D. M. Meyer, J. A. Cardelli, and U. J. Sofia, Astrophys. J. **490**, L103 (1997).
[4] G. Wallerstein, I. Iben, P. Parker, A. Boesgaard, G. Hale, A. Champagne, C. Barnes, F. Käppeler, V. Smith, R. Hoffman, et al., Rev. Mod. Phys. **69**, 995 (1997).
[5] K. Lodders and J. B. Fegley, Icarus **155**, 393 (2002).
[6] W. B. Hubbard, *Planetary Interiors* (University of Arizona Press, Tucson, AZ, 1984).

[7] W. J. Nellis, H. B. Radousky, D. C. Hamilton, a. C. Mitchell, N. C. Holmes, K. B. Christianson, and M. van Thiel, J. Chem. Phys. **94**, 2244 (1991).
[8] M. Ross and F. Rogers, Phys. Rev. B **74**, 024103 (2006).
[9] B. Boates and S. a. Bonev, Phys. Rev. Lett. **102**, 015701 (2009).
[10] R. Reichlin, D. Schiferl, S. Martin, C. Vanderborgh, and R. L. Mills, Phys. Rev. Lett. **55**, 1464 (1985).
[11] R. L. Mills, B. Olinger, and D. T. Cromer, J. Chem. Phys. **84**, 2837 (1986).
[12] H. Olijnyk, J. Chem. Phys. **93**, 8968 (1990).
[13] R. Bini, L. Ulivi, J. Kreutz, and H. J. Jodl, J. Chem. Phys. **112**, 8522 (2000).
[14] E. Gregoryanz, A. F. Goncharov, R. J. Hemley, H. k. Mao, M. Somayazulu, and G. Shen, Phys. Rev. B **66**, 224108 (2002).
[15] E. Gregoryanz, A. F. Goncharov, C. Sanloup, M. Somayazulu, H. K. Mao, and R. J. Hemley, J. Chem. Phys. **126**, 184505 (2007).
[16] A. K. McMahan and R. LeSar, Phys. Rev. Lett. **54**, 1929 (1985).
[17] R. M. Martin and R. J. Needs, Phys. Rev. B **34**, 5082 (1986).
[18] C. Mailhiot, L. H. Yang, and a. K. McMahan, Phys. Rev. B **46**, 14419 (1992).
[19] H. K. an dP. Toledano, Phys. Rev. B **78**, 064103 (2008).
[20] C. J. Pickard and R. J. Needs, Phys. Rev. Lett. **102**, 125702 (2009).
[21] A. Erba, L. Maschio, C. Pisani, and S. Casassa, Phys. Rev. B **84**, 012101 (2011).
[22] A. F. Goncharov, E. Gregoryanz, H. K. Mao, Z. Liu, and R. J. Hemley, Phys. Rev. Lett. **85**, 1262 (2000).
[23] M. I. Eremets, R. J. Hemley, Mao Hk, and E. Gregoryanz, Nature **411**, 170 (2001).
[24] E. Gregoryanz, A. F. Goncharov, R. J. Hemley, and H. k. Mao, Phys. Rev. B **64**, 052103 (2001).
[25] M. I. Eremets, A. G. Gavriliuk, I. a. Trojan, D. a. Dzivenko, and R. Boehler, Nat. Mater. **3**, 558 (2004).
[26] M. I. Eremets, a. G. Gavriliuk, N. R. Serebryanaya, I. a. Trojan, D. a. Dzivenko, R. Boehler, H. K. Mao, and R. J. Hemley, J. Chem. Phys. **121**, 11296 (2004).
[27] M. Popov, Phys. Lett. A **334**, 317 (2005).
[28] M. J. Lipp, J. P. Klepeis, B. J. Baer, H. Cynn, W. J. Evans, V. Iota, and C.-S. Yoo, Phys. Rev. B **76**, 014113 (2007).
[29] M. I. Eremets, a. G. Gavriliuk, and I. a. Trojan, Appl. Phys. Lett. **90**, 6 (2007).
[30] X.-Q. Chen, C. L. Fu, and R. Podloucky, Phys. Rev. B **77**, 064103 (2008).
[31] W. D. Mattson, D. Sanchez-Portal, S. Chiesa, and R. M. Martin, Phys. Rev. Lett. **93**, 125501 (2004).
[32] F. Zahariev, a. Hu, J. Hooper, F. Zhang, and T. Woo, Phys. Rev. B **72**, 2 (2005).
[33] F. Zahariev, S. V. Dudiy, J. Hooper, F. Zhang, and T. K. Woo, Phys. Rev. Lett. **97**, 155503 (2006).
[34] X. L. Wang, Z. He, Y. M. Ma, T. Cui, Z. M. Liu, B. B. Liu, J. F. Li, and G. T. Zou, J. Phys. Condens. Matter **19**, 425226 (2007).
[35] Y. Yao, J. S. Tse, and K. Tanaka, Phys. Rev. B **77**, 052103 (2008).
[36] Y. Ma, A. R. Oganov, Z. Li, Y. Xie, and J. Kotakoski, Phys. Rev. Lett. **102**, 100 (2009).
[37] X. Wang, F. Tian, L. Wang, T. Cui, B. Liu, and G. Zou, J. Chem. Phys. **132**, 024502 (2010).
[38] B. Boates and S. a. Bonev, Phys. Rev. B **83**, 174114 (2011).
[39] X. Wang, Y. Wang, M. Miao, X. Zhong, J. Lv, T. Cui, J. Li, L. Chen, C. J. Pickard, and Y. Ma, Phys. Rev. Lett. **109**, 175502 (2012).
[40] V. N. Zubarev and G. S. Telegin, Dokl. Akad. Nauk SSSR **142**, 309 (1962).
[41] R. D. Dick, J. Chem. Phys. **52**, 6021 (1970).
[42] W. J. Nellis and A. C. Mitchell, J. Chem. Phys. **73**, 6137 (1980).
[43] W. J. Nellis, N. C. Holmes, A. C. Mitchell, and M. van Thiel, Phys. Rev. Lett. **53**, 1661 (1984).
[44] G. Schott, M. S. Shaw, and J. D. Johnson, J. Chem. Phys. **82**, 4264 (1985).
[45] H. B. Radousky, W. J. Nellis, M. Ross, D. C. Hamilton, and a. C. Mitchell, Phys. Rev. Lett. **57**, 2419 (1986).
[46] D. S. Moore, S. C. Schmidt, M. S. Shaw, and J. D. Johnson, J. Chem. Phys. **90**, 1368 (1989).
[47] R. Chau, a. Mitchell, R. Minich, and W. Nellis, Phys. Rev. Lett. **90**, 245501 (2003).
[48] M. Ross and F. H. Ree, J. Chem. Phys. **73**, 6146 (1980).
[49] M. Ross, J. Chem. Phys. **86**, 7110 (1987).
[50] Ross, High Press. Res. **10**, 649 (1992).
[51] Q. F. Chen, L. C. Cai, Y. Zhang, Y. J. Gu, and F. Q. Jing, J. Chem. Phys. **124**, 074510 (2006).
[52] J. D. Johnson, M. S. Shaw, and B. L. Holian, J. Chem. Phys. **80**, 1279 (1983).
[53] G. I. Kerley and A. C. Switendick, in *Shock Waves Condens. Matter*, edited by Y. M. Gupta (Plenum Press, New York, 1986), 1, pp. 95–100.
[54] D. C. Hamilton and F. H. Ree, J. Chem. Phys. **90**, 4972 (1989).
[55] M. V. Thiel and F. H. Ree, J. Chem. Phys. **104**, 5019 (1996).
[56] J. Belak, R. D. Etters, and R. LeSar, J. Chem. Phys. **89**, 1625 (1988).
[57] L. E. Fried and W. M. Howard, J. Chem. Phys. **109**, 7338 (1998).
[58] J. D. Kress, S. Mazevet, L. A. Collins, and W. W. Wood, Phys. Rev. B **61**, 024203 (2000).
[59] S. Mazevet, J. Johnson, J. Kress, L. Collins, and P. Blottiau, Phys. Rev. B **65**, 014204 (2001).
[60] W. D. Mattson and R. Balu, Phys. Rev. B **83**, 174105 (2011).
[61] F. Rogers and D. A. Young, Phys. Rev. E **56**, 5876 (1997).
[62] B. F. Rozsnyai, J. R. Albritton, D. A. Young, V. N. Sonnad, and D. A. Liberman, Phys. Lett. A **291**, 226 (2001).
[63] C. Pierleoni, D. M. Ceperley, B. Bernu, and W. R. Magro, Phys. Rev. Lett. **73**, 2145 (1994).
[64] W. R. Magro, D. M. Ceperley, C. Pierleoni, and B. Bernu, Phys. Rev. Lett. **76**, 1240 (1996).
[65] B. Militzer, W. Magro, and D. Ceperley, Contr. Plasma Physics **39**, 151 (1999).
[66] B. Militzer and D. M. Ceperley, Phys. Rev. Lett. **85**, 1890 (2000).
[67] B. Militzer and D. M. Ceperley, Phys. Rev. E **63**, 066404 (2001).
[68] B. Militzer, D. M. Ceperley, J. D. Kress, J. D. Johnson, L. A. Collins, and S. Mazevet, Phys. Rev. Lett. **87**, 275502 (2001).
[69] B. Militzer, Phys. Rev. Lett. **97**, 175501 (2006).
[70] B. Militzer, Phys. Rev. B **79**, 155105 (2009).
[71] B. Militzer, J Phys. A **42**, 214001 (2009).
[72] K. P. Driver and B. Militzer, Phys. Rev. Lett. **108**, 115502

(2012).
[73] L. X. Benedict, K. P. Driver, S. Hamel, B. Militzer, T. Qi, A. A. Correa, and E. Schwegler, Phys. Rev. B **89**, 224109 (2014).
[74] K. P. Driver, F.Soubiran, S. Zhang, and B. Militzer, J. Chem. Phys. **143**, 164507 (2015).
[75] K. P. Driver and B. Militzer, Phys. Rev. B **91**, 045103 (2015).
[76] B. Militzer and K. P. Driver, Phys. Rev. Lett. **115**, 176403 (2015).
[77] D. M. Ceperley, J. Stat. Phys. **63**, 1237 (1991).
[78] D. M. Ceperley, Rev. Mod. Phys. **67**, 279 (1995).
[79] D. M. Ceperley, in *Monte Carlo and Molecular Dynamics of Condensed Matter Systems*, edited by E. K. Binder and G. Ciccotti (Editrice Compositori, Bologna, Italy, 1996).
[80] M. Koenig *et al.*, Plasma Phys. Contr. F. **47**, B441 (2005).
[81] E. L. Pollock, Comput. Phys. Commun. **52**, 49 (1988).
[82] B. Militzer and R. L. Graham, J. Phys. Chem. Solids **67**, 2143 (2006).
[83] D. M. Ceperley, J. Stat. Phys. **63**, 1237 (1991).
[84] See supplemental material at [URL] for the EOS table.
[85] D. Marx and J. Hutter, in *Modern Methods and Algorithms of Quantum Chemistry Proceedings*, edited by J. Grotendorst (NIC Series, Julich, Germany, 2000), vol. 3, pp. 301–449.
[86] E. W. Brown, B. K. Clark, J. L. DuBois, and D. M. Ceperley, Phys. Rev. Lett. **110**, 146405 (2013).
[87] D. N. Mermin, Phys. Rev. **137**, A1441 (1965).
[88] F. Lambert, J. Clérouin, and G. Zérah, Phys. Rev. E **73**, 016403 (2006).
[89] F. Lambert, J. Clérouin, S. Mazevet, and D. Gilles, Contrib. Plasma Phys. **47**, 272 (2007).
[90] V. V. Karasiev, D. Chakraborty, O. A. Shukruto, and S. B. Trickey, Phys. Rev. B **88**, 161108(R) (2013).
[91] T. Sjostrom and J. Daligault, Phys. Rev. Lett. **113**, 155006 (2014).
[92] B. F. Rozsnyai, High. Energy Dens. Phys. **16**, 407 (2014).
[93] C. E. Starrett, J. Daligault, and D. Saumon, Phys. Rev. E **91**, 013104 (2015).
[94] G. Kresse and J. Furthmüller, Phys. Rev. B **54**, 11169 (1996).
[95] P. E. Blöchl, Phys. Rev. B **50**, 17953 (1994).
[96] J. P. Perdew, K. Burke, and M. Ernzerhof, Phys. Rev. Lett. **77**, 3865 (1996).
[97] `http://opium.sourceforge.net`.
[98] D. A. Young, C.-S.Zha, R. Boehler, J. Yen, M. Nicol, A. S. Zinn, D. Schiferl, S. Kinkead, R. C. Hanson, and D. A. Pinnick, Phys. Rev. B **35**, 5353 (1987).
[99] G. D. Mukherjee and R. Boehler, Phys. Rev. Lett. **99**, 225701 (2007).
[100] A. F. Goncharov, J. C. Crowhurst, V. V. Struzhkin, and R. J. Hemley, Phys. Rev. Lett. **101**, 095502 (2008).
[101] D. Donadio, L. Spanu, I. Duchemin, F. Gygi, and G. Galli, Phys. Rev. B **82**, 020102(R) (2010).
[102] W. Ebeling, W. Kraeft, and D. Kremp, *Theory of bound states and ionization equilibrium in plasmas and solids* (Akademie-Verlag, Berlin, 1976).
[103] P. Debye and E. Huckel, Phys. Z. **24**, 185 (1923).
[104] L. Landau, E. Lifšic, H. Sykes, and M. Kearsley, *Statistical Physics*, Course of Theoretical Physics (Elsevier Science & Technology, 1980).
[105] B. Militzer, J. Phys. A: Math. Theor. **42**, 214001 (2009).
[106] S. Root, R. J. Magyar, J. H. Carpenter, D. L. Hanson, and T. R. Mattsson, Phys. Rev. Lett. **105**, 085501 (2010).
[107] T. R. Mattsson, S. Root, A. E. Mattsson, L. Shulenburger, R. J. Magyar, and D. G. Flicker, Phys. Rev. B **90**, 184105 (2014).
[108] Y. B. Zel'dovich and Y. P. Raizer, *Elements of Gasdynamics and the Classical Theory of Shock Waves* (Academic Press, New York, 1968).
[109] J. A. Venables and C. A. English, Acta Crystallogr. Sect. B **30**, 929 (1973).
[110] B. Militzer and W. B. Hubbard, AIP Conf. Proc. **955**, 1395 (2007).
[111] Y. B. Zel'dovich and Y. P. Raizer, *Physics of Shock Waves and High-Temperature Hydrodynamic Phenomena*, Dover Books on Physics (Dover Publications, 2002).

arXiv:1601.05787v1 [physics.plasm-ph] 21 Jan 2016

First-Principles Equation of State Calculations of Warm Dense Nitrogen

K. P. Driver[1,*] and B. Militzer[1,2]

[1]*Department of Earth and Planetary Science, University of California, Berkeley, California 94720, USA*
[2]*Department of Astronomy, University of California, Berkeley, California 94720, USA*

(Dated: January 23, 2016)

TABLE I: Nitrogen EOS table of pressures and internal energies at density-temperature conditions simulated in this work. Relativistic corrections are included for $T \geq 8 \times 10^6$ K. The numbers in parentheses indicate one-sigma statistical uncertainties of the DFT-MD and PIMC simulations.

Method	T (K)	P (GPa)	E (Ha/atom)
$\rho = 1.50000$ g cm^{-3}			
DFT-MD	1000	7.56(7)	−54.6030(1)
DFT-MD	2000	9.71(8)	−54.5953(1)
DFT-MD	2500	10.49(8)	−54.5917(1)
DFT-MD	3500	12.3(1)	−54.5843(2)
DFT-MD	5000	14.3(2)	−54.5741(3)
DFT-MD	6000	15.3(1)	−54.5663(3)
DFT-MD	7500	16.3(3)	−54.5502(8)
DFT-MD	10000	17.1(1)	−54.511(1)
DFT-MD	15000	19.1(2)	−54.422(2)
DFT-MD	20000	26.5(3)	−54.349(1)
DFT-MD	30000	45.5(5)	−54.226(1)
DFT-MD	40000	65.7(4)	−54.0940(9)
DFT-MD	50000	88.1(7)	−53.9448(9)
$\rho = 1.62000$ g cm^{-3}			
DFT-MD	1000	9.64(5)	−54.6013(1)
DFT-MD	2000	11.85(7)	−54.5932(1)
DFT-MD	2500	12.66(5)	−54.5892(8)
DFT-MD	3500	14.5(1)	−54.5820(1)
DFT-MD	5000	16.9(1)	−54.5699(2)
DFT-MD	6000	18.2(1)	−54.5616(1)
DFT-MD	7500	19.8(2)	−54.5488(3)
DFT-MD	10000	19.4(2)	−54.503(1)
DFT-MD	15000	22.7(3)	−54.422(1)
DFT-MD	20000	30.1(3)	−54.350(1)
DFT-MD	30000	50.6(4)	−54.2267(5)
DFT-MD	40000	73.3(3)	−54.0987(8)
DFT-MD	50000	98.7(5)	−53.9528(6)
$\rho = 1.75000$ g cm^{-3}			
DFT-MD	2000	15.39(9)	−54.5911(1)
DFT-MD	2500	16.47(7)	−54.5872(1)
DFT-MD	3500	18.6(1)	−54.5791(1)
DFT-MD	5000	20.6(1)	−54.5679(2)
DFT-MD	6000	22.4(1)	−54.5595(2)
DFT-MD	7500	23.2(3)	−54.5418(7)
DFT-MD	10000	22.7(2)	−54.498(1)
DFT-MD	15000	26.4(5)	−54.420(2)
DFT-MD	20000	35.0(4)	−54.3539(9)
DFT-MD	30000	57.7(6)	−54.231(1)

*Electronic address: kdriver@berkeley.edu; URL: http://militzer.berkeley.edu/~driver/

Table I *Continued*.

Method	T (K)	P (GPa)	E (Ha/atom)
DFT-MD	40000	82.6(6)	−54.1030(7)
DFT-MD	50000	108.6(6)	−53.9581(6)
$\rho = 1.87000$ g cm^{-3}			
DFT-MD	2000	18.6(1)	−54.5887(1)
DFT-MD	2500	20.1(1)	−54.5847(1)
DFT-MD	3500	22.3(1)	−54.5775(1)
DFT-MD	5000	24.9(1)	−54.5659(2)
DFT-MD	6000	26.2(2)	−54.5570(3)
DFT-MD	7500	27.5(2)	−54.5390(5)
DFT-MD	10000	25.7(3)	−54.494(2)
DFT-MD	15000	29.9(2)	−54.417(1)
DFT-MD	20000	38.9(2)	−54.3538(9)
DFT-MD	30000	63.5(6)	−54.2350(8)
DFT-MD	40000	92.3(4)	−54.1083(8)
DFT-MD	50000	120(1)	−53.9642(6)
$\rho = 2.0000$ g cm^{-3}			
DFT-MD	2000	22.60(8)	−54.5856(1)
DFT-MD	2500	22.1(1)	−54.5802(2)
DFT-MD	3500	25.7(1)	−54.5725(1)
DFT-MD	5000	29.2(1)	−54.5605(2)
DFT-MD	6000	30.6(2)	−54.5512(5)
DFT-MD	7500	29.9(3)	−54.529(2)
DFT-MD	10000	29.5(2)	−54.4880(8)
DFT-MD	15000	34.1(3)	−54.4172(9)
DFT-MD	20000	45.3(4)	−54.3537(8)
DFT-MD	30000	72.8(6)	−54.2365(7)
DFT-MD	40000	100.7(6)	−54.1097(8)
DFT-MD	50000	133.2(9)	−53.9718(7)
$\rho = 2.12000$ g cm^{-3}			
DFT-MD	2000	27.42(6)	−54.5831(1)
DFT-MD	2500	28.7(1)	−54.5790(1)
DFT-MD	3500	31.6(1)	−54.5703(2)
DFT-MD	5000	34.2(1)	−54.5574(3)
DFT-MD	6000	35.3(2)	−54.5475(5)
DFT-MD	7500	35.1(4)	−54.526(2)
DFT-MD	10000	33.9(4)	−54.482(1)
DFT-MD	15000	38.8(4)	−54.4143(8)
DFT-MD	20000	50.9(5)	−54.356(1)
DFT-MD	30000	80.0(7)	−54.2395(7)
DFT-MD	40000	110.9(6)	−54.1146(6)
DFT-MD	50000	144(1)	−53.9737(5)
$\rho = 2.25000$ g cm^{-3}			
DFT-MD	2000	32.6(1)	−54.5798(1)
DFT-MD	2500	34.3(1)	−54.5751(1)
DFT-MD	3500	37.4(1)	−54.5673(2)
DFT-MD	5000	41.1(1)	−54.5540(2)
DFT-MD	6000	40.9(3)	−54.5403(6)
DFT-MD	7500	39.3(4)	−54.518(1)
DFT-MD	10000	37.1(2)	−54.4776(6)
DFT-MD	15000	44.7(5)	−54.413(1)
DFT-MD	20000	56.8(4)	−54.3568(7)
DFT-MD	30000	89.7(8)	−54.2396(9)
DFT-MD	40000	123.2(9)	−54.1161(8)
DFT-MD	50000	157.9(7)	−53.9789(4)

Table I *Continued*.

Method	T (K)	P (GPa)	E (Ha/atom)
$\rho = 2.42000$ g cm^{-3}			
DFT-MD	2500	41.88(8)	−54.5701(1)
DFT-MD	3500	46.1(1)	−54.5618(1)
DFT-MD	5000	49.1(2)	−54.5476(3)
DFT-MD	6000	48.2(4)	−54.5336(7)
DFT-MD	7500	45.3(5)	−54.508(1)
DFT-MD	10000	43.8(4)	−54.4711(7)
DFT-MD	15000	52.9(5)	−54.4117(6)
DFT-MD	20000	67.0(5)	−54.355(9)
DFT-MD	30000	102.7(4)	−54.2410(7)
DFT-MD	40000	139.6(6)	−54.1185(5)
DFT-MD	50000	179(1)	−53.9814(8)

Table I *Continued*.

Method	T (K)	P (GPa)	E (Ha/atom)	$P_{relativistic}$ (GPa)	$E_{relativistic}$ (Ha/atom)
$\rho = 2.52736$ g cm^{-3}					
DFT-MD	2500	47.7(1)	−54.5671(1)		
DFT-MD	3500	51.0(1)	−54.5581(1)		
DFT-MD	5000	54.0(1)	−54.5434(2)		
DFT-MD	6000	52.9(5)	−54.5280(6)		
DFT-MD	7500	49.8(3)	−54.5051(8)		
DFT-MD	10000	49.0(3)	−54.4693(5)		
DFT-MD	15000	58.8(5)	−54.4095(5)		
DFT-MD	20000	74.1(4)	−54.355(7)		
DFT-MD	30000	111.3(5)	−54.241(7)		
DFT-MD	40000	147.4(6)	−54.1205(3)		
DFT-MD	50000	191.4(9)	−53.9856(4)		
DFT-MD	100000	429(1)	−53.098(1)		
DFT-MD	250000	1383(3)	−49.389(2)		
PIMC	500000	3292(12)	−41.71(4)		
DFT-MD	500000	3326(5)	−42.16(1)		
PIMC	748503	5433(11)	−34.12(3)		
DFT-MD	750000	5458(7)	−34.68(2)		
PIMC	998004	7727(9)	−24.98(5)		
DFT-MD	1000000	7790(5)	−26.71(2)		
PIMC	2020960	19466(14)	31.69(5)		
PIMC	4041920	45180(12)	130.12(4)		
PIMC	8083850	94496(30)	290.7(1)	94496	291.2
PIMC	16167700	192028(68)	601.0(2)	192028	602.8
PIMC	49746542	595296(310)	1879(1)	595296	1896
PIMC	99497670	1192049(654)	3769(2)	1192053	3837
PIMC	1034730000	12417450(1044)	39312(3)	12417492	45648

Table I *Continued*.

Method	T (K)	P (GPa)	E (Ha/atom)
$\rho = 2.75000$ g cm^{-3}			
DFT-MD	2500	60.9(1)	−54.5604(2)
DFT-MD	3500	64.5(1)	−54.5497(2)
DFT-MD	5000	64.2(6)	−54.5312(8)
DFT-MD	6000	61.4(4)	−54.5160(5)
DFT-MD	7500	58.2(2)	−54.4941(2)
DFT-MD	10000	59.0(2)	−54.4624(5)
DFT-MD	15000	71.8(3)	−54.4062(5)

Table I *Continued*.

Method	T (K)	P (GPa)	E (Ha/atom)
DFT-MD	20000	88.4(4)	−54.3519(4)
DFT-MD	30000	130.3(7)	−54.2425(4)
DFT-MD	40000	171.7(8)	−54.1227(5)
DFT-MD	50000	218.5(5)	−53.9871(3)
$\rho = 2.90880$ g cm^{-3}			
DFT-MD	2500	71.1(1)	−54.5533(2)
DFT-MD	3500	75.1(2)	−54.5434(3)
DFT-MD	5000	70.1(5)	−54.5213(6)
DFT-MD	6000	65.6(4)	−54.5055(4)
DFT-MD	7500	64.4(3)	−54.4863(5)
DFT-MD	10000	68.2(3)	−54.4567(4)
DFT-MD	15000	82.5(5)	−54.4039(3)
DFT-MD	20000	101.9(4)	−54.3504(5)
DFT-MD	30000	145.3(5)	−54.2422(4)
DFT-MD	40000	190.9(7)	−54.1214(5)
DFT-MD	50000	239.0(8)	−53.9889(5)
$\rho = 3.00000$ g cm^{-3}			
DFT-MD	2500	77.3(1)	−54.5502(1)
DFT-MD	3500	80.3(4)	−54.5390(4)
DFT-MD	5000	73.0(5)	−54.5157(4)
DFT-MD	6000	70.4(4)	−54.5021(3)
DFT-MD	7500	69.0(3)	−54.4825(4)
DFT-MD	10000	73.2(2)	−54.4544(3)
DFT-MD	15000	89.1(4)	−54.4017(5)
DFT-MD	20000	109.2(5)	−54.3489(3)
DFT-MD	30000	154.6(7)	−54.2408(4)
DFT-MD	40000	202.3(7)	−54.1207(3)
DFT-MD	50000	253.0(9)	−53.9883(5)
$\rho = 3.25000$ g cm^{-3}			
DFT-MD	2500	95.5(1)	−54.5396(1)
DFT-MD	3500	89.4(7)	−54.5245(2)
DFT-MD	5000	81.2(3)	−54.5033(2)
DFT-MD	6000	80.9(3)	−54.4912(3)
DFT-MD	7500	83.0(4)	−54.4739(3)
DFT-MD	10000	90.4(3)	−54.4469(2)
DFT-MD	15000	109.7(3)	−54.3968(3)
DFT-MD	20000	131.3(5)	−54.3456(4)
DFT-MD	30000	182.2(5)	−54.2374(3)
DFT-MD	40000	234.6(9)	−54.1195(4)
DFT-MD	50000	288(1)	−53.9897(7)
$\rho = 3.50000$ g cm^{-3}			
DFT-MD	2500	97.1(6)	−54.5264(2)
DFT-MD	3500	93.0(6)	−54.5116(2)
DFT-MD	5000	94.0(3)	−54.4931(2)
DFT-MD	6000	96.5(2)	−54.4817(1)
DFT-MD	7500	100.5(2)	−54.4654(3)
DFT-MD	10000	109.9(3)	−54.4403(2)
DFT-MD	15000	133.3(4)	−54.3899(5)
DFT-MD	20000	157.8(6)	−54.3400(4)
DFT-MD	30000	213.3(6)	−54.2332(5)
DFT-MD	40000	269.1(7)	−54.1170(6)
DFT-MD	50000	330(1)	−53.9865(5)

Table I *Continued*.

Method	T (K)	P (GPa)	E (Ha/atom)	$P_{relativistic}$ (GPa)	$E_{relativistic}$ (Ha/atom)
$\rho = 3.70586$ g cm^{-3}					
DFT-MD	2500	92.3(6)	−54.5207(3)		
DFT-MD	3500	100.1(7)	−54.5038(2)		
DFT-MD	5000	107.1(3)	−54.4859(2)		
DFT-MD	6000	111.2(2)	−54.4746(1)		
DFT-MD	7500	117.5(3)	−54.4588(2)		
DFT-MD	10000	129.0(3)	−54.4339(3)		
DFT-MD	15000	155.2(4)	−54.3847(3)		
DFT-MD	20000	182.0(5)	−54.3345(3)		
DFT-MD	30000	240.1(6)	−54.2293(4)		
DFT-MD	40000	301.8(9)	−54.1128(5)		
DFT-MD	50000	364.1(8)	−53.9859(4)		
DFT-MD	100000	736(4)	−53.156(2)		
PIMC	250000	2041(25)	−49.03(5)		
DFT-MD	250000	2128(5)	−49.674(3)		
PIMC	500000	4906(17)	−42.23(3)		
DFT-MD	500000	4919(9)	−42.82(1)		
PIMC	748503	7900(19)	−35.09(4)		
DFT-MD	750000	8002(14)	−35.50(3)		
PIMC	998004	11155(20)	−26.47(5)		
DFT-MD	1000000	11388(25)	−27.67(7)		
PIMC	2020960	27900(20)	26.71(5)		
PIMC	4041920	65381(16)	125.62(4)		
PIMC	8083850	138020(36)	288.00(9)	138020	288.4
PIMC	16167700	280934(109)	598.5(2)	280934	600.3
PIMC	49746542	872493(429)	1877.3(9)	872492	1894.5
PIMC	99497670	1748778(888)	3770(2)	1748783	3838
PIMC	1034730000	18205150(1897)	39306(4)	18205208	45642
$\rho = 7.82952$ g cm^{-3}					
DFT-MD	10000	1116(2)	−54.183(1)		
DFT-MD	50000	1661(4)	−53.757(2)		
DFT-MD	100000	2413(4)	−53.050(1)		
PIMC	250000	5385(54)	−48.80(5)		
DFT-MD	250000	5342(9)	−49.964(4)		
PIMC	500000	10758(41)	−43.28(4)		
DFT-MD	500000	11150(15)	−43.61(1)		
PIMC	748503	17030(42)	−36.49(4)		
DFT-MD	750000	17366(27)	−36.81(2)		
PIMC	998004	23651(30)	−28.73(3)		
DFT-MD	1000000	24111(42)	−29.55(5)		
PIMC	2020960	56615(47)	17.53(5)		
PIMC	4041920	134303(34)	115.31(4)		
PIMC	8083850	288195(112)	280.5(1)	288194	280.9
PIMC	16167700	587988(204)	589.4(2)	587987	591.2
PIMC	49746542	1841498(1014)	1873(1)	1841498	1890
PIMC	99497670	3694944(1982)	3786(2)	3694944	3837
PIMC	1034730000	38463564(3144)	39305(3)	38463672	45641
$\rho = 13.9462$ g cm^{-3}					
DFT-MD	10000	4526(12)	−53.608(2)		
DFT-MD	50000	5734(5)	−53.108(1)		
DFT-MD	100000	7032(8)	−52.473(2)		
PIMC	250000	13170(99)	−47.68(5)		
DFT-MD	250000	12028(9)	−49.696(3)		
PIMC	500000	20971(69)	−43.59(4)		
DFT-MD	500000	22039(20)	−43.778(8)		
PIMC	748503	32093(77)	−36.97(4)		
DFT-MD	750000	32787(23)	−37.34(1)		
PIMC	998004	43128(68)	−29.99(4)		

Table I *Continued*.

Method	T (K)	P (GPa)	E (Ha/atom)	$P_{relativistic}$ (GPa)	$E_{relativistic}$ (Ha/atom)
DFT-MD	1000000	44391(82)	−30.41(5)		
PIMC	2020960	99060(65)	11.48(4)		
PIMC	4041920	233718(56)	106.13(4)		
PIMC	8083850	508193(153)	273.4(1)	508193	273.9
PIMC	16167700	1049077(357)	587.9(2)	1049077	589.7
PIMC	49746542	3277237(1514)	1869.6(9)	3277237	1886.8
PIMC	99497670	6577836(2765)	3764(2)	6577836	3832
PIMC	1034730000	68515111(6897)	39305(4)	68515322	45641